FORMATION OF DWARF GALAXIES DURING THE COSMIC REIONIZATION

Hajime Susa

Department of Physics, Rikkyo University, Nishi-Ikebukuro, Toshimaku, Japan; susa@rikkyo.ac.jp

AND

Masayuki Umemura

Center for Computational Physics, University of Tsukuba, Japan; umemura@rccp.tsukuba.ac.jp

ABSTRACT

We reanalyze the photoevaporation problem of subgalactic objects irradiated by ultraviolet background (UVB) radiation in a reionized universe. For the purpose, we perform three-dimensional radiation smoothed particle hydrodynamics (RSPH) calculations, in which the radiative transfer is solved by a direct method and the nonequilibrium chemistry of primordial gas including H_2 molecules is also incorporated. Attention is concentrated on radiative transfer effects on the UVB for the formation of subgalactic objects with $T_{vir} \lesssim 10^4$ K. We consider a reionization model with $z_{reion} \approx 7$ and also the earlier reionization model ($z_{reion} \approx 17$) inferred by the *Wilkinson Microwave Anisotropy Probe* (*WMAP*). We find that star formation is suppressed appreciably by UVB, but baryons at high-density peaks are self-shielded even during the reionization, forming some amount of stars eventually. In that sense, the photoevaporation for subgalactic systems is not as perfect as argued by one-dimensional spherical calculations. The final stellar fraction depends on the collapse epoch and the mass of the system, almost regardless of the reionization epoch. For instance, a few tenths of the formed stars are born after the cosmic reionization in the $z_{reion} \approx 7$ model, while more than 90% of the stars are born after the reionization in the *WMAP* reionization model. Thus, the effects of UVB feedback on the substructure problem with a cold dark matter (CDM) scenario should be evaluated with careful treatment of the radiative transfer. The star clusters formed at high-density peaks coalesce with each other in a dissipationless fashion in a dark matter potential, as a resultant forming a spheroidal system. As a result, these low-mass galaxies have large mass-to-light ratios, such as observed in dwarf spheroidal galaxies in the Local Group.

Subject headings: galaxies: dwarf — galaxies: formation — hydrodynamics — molecular processes — radiative transfer

On-line material: color figures

1. INTRODUCTION

In the context of cold dark matter (CDM) cosmology, the first generation of objects should have a mass of $\sim 10^6\, M_\odot$ and form at redshifts of $20 \lesssim z \lesssim 50$ (Tegmark et al. 1997; Fuller & Couchman 2000). At later epochs, the first objects are assembled into larger systems in a hierarchical fashion, to form dwarf or normal galaxies. On the other hand, it is thought that the universe was reionized at $z > 5$, because the absorption by the neutral intergalactic medium (IGM) is observed to be feeble at redshifts $z \lesssim 4$. The reionization redshift is inferred to be $z_{reion} \approx 6$ from the spectra of high-z quasars (Djorgovski et al. 2001 and references therein), $6 \lesssim z_{reion} \lesssim 10$ from simulations of Lyα absorption lines (Umemura, Nakamoto, & Susa 2001), or $11 \lesssim z_{reion} \lesssim 30$ from the recent results of the *Wilkinson Microwave Anisotropy Probe* (*WMAP*; Kogut et al. 2003). Thus, it is anticipated that the ultraviolet background (UVB) directly influences the assembly phase of galaxies. The UVB has several important physical effects on galaxy formation. One of the most important effects is photoheating. If a gas cloud is irradiated by the UVB, the gas temperature is raised up to $T \sim 10^4$–10^5 K, so that gaseous systems with a virial temperature of $T \lesssim 10^4$ K can be evaporated owing to the enhanced thermal pressure (Umemura & Ikeuchi 1984; Dekel & Rees 1987; Efstathiou 1992; Babul & Rees 1992; Thoul & Weinberg 1996; Ferrara & Tolstoy 2000; Gnedin 2000b;

Shapiro & Raga 2001; Shaviv & Dekel 2003). Such an effect by the UVB may reconcile the paradox that low-mass galaxies are overproduced in CDM cosmology, compared with observations (White & Frenk 1991; Kauffmann, White, & Guiderdoni 1993; Cole et al. 1994; Moore et al. 1999; Binney, Gerhard, & Silk 2001). The criterion for photoevaporation has been derived from detailed hydrodynamic calculations by Umemura & Ikeuchi (1984) and Thoul & Weinberg (1996). However, if the systems are self-shielded against the UVB, the criterion for photoevaporation is completely changed. The self-shielding comes from the radiative transfer effects of ionizing photons. Tajiri & Umemura (1998) have derived the self-shielding criterion by solving full radiative transfer for spherical clouds, to find a critical optical depth of 2.4. In addition, if the system is self-shielded from the UVB, the gas can cool below 10^4 K by H_2 cooling (Susa & Kitayama 2000). Complete radiation-hydrodynamic calculations have been done for spherical clouds by Kitayama et al. (2001), in which hydrodynamics, radiative transfer, and primordial gas chemistry including H_2 molecules are self-consistently incorporated, and thereby the criteria for cloud collapse have been derived depending on the redshifts. Very recently, pioneering approaches with three-dimensional hydrodynamics have started on this issue in the context of CDM cosmology. They are, for example, the simulations by Ricotti, Gnedin, & Shull (2002a, 2002b), with radiative transfer

based on the optically thin variable Eddington tensor (OTVET) approximation, and by Tassis et al. (2003), with an optically thin approximation.

If the nonlinear evolution of density fluctuations proceeds in a hierarchical fashion, two major effects of radiative transfer are expected. One is the direct effect, that is, the self-shielding of density peaks that collapse prior to the reionization (Gnedin 2000b; Nakamoto, Umemura, & Susa 2001; Razoumov et al. 2002; Ricotti et al. 2002a, 2002b). The other is the enhancement of H_2 formation in relatively massive fluctuations that are ionized once and then self-shielded in the course of mass accretion. The second effect has been pointed out by many authors so far (Kang & Shapiro 1992; Corbelli, Galli, & Palla 1997; Susa & Umemura 2000a). These two effects play a substantial role in galaxy formation under the UVB, especially if the star formation process is taken into account in collapsing clouds, because star formation activities in galaxies appear to be strongly correlated to cold H I gas with a few times 10^3 K (Young & Lo 1997a, 1997b). Therefore, the effects of radiation transfer of ionizing photons should be carefully treated to elucidate the galaxy formation process under the UVB. In this paper, we perform three-dimensional smoothed particle hydrodynamics (SPH) calculations, incorporating radiation transfer and primordial gas chemistry. Here we focus on relatively low mass galaxies, where the dynamics is likely to be strongly subject to the UVB. The evolution of subgalactic systems is also significant for the formation of massive galaxies, since the self-shielding against the UVB can be responsible for the overall star formation history (SFH) in the galaxies and therefore the resultant galactic morphology (Susa & Umemura 2000b).

The goal of this paper is to elucidate how the photo-evaporation of subgalactic systems is caused by the UVB and how the SFH is influenced consequently. The paper is organized as follows: In § 2, the numerical methods are described. In § 3, the results of simulations are presented. In § 4, the SFH is discussed in relation to the inferred SFH in dwarf galaxies. Section 5 is devoted to the conclusions.

2. NUMERICAL METHODS

We have performed numerical simulations of a single-halo collapse with SPH particles (2^{15}) and dark matter particles (2^{15}). The halo mass ranges from $M_{halo} \approx 6 \times 10^7$ to 6×10^8 $M_\odot$. The initial conditions are set by COSMICS. The radiative transfer of the UV radiation field is solved assuming a single source outside the simulation box, coupled with the detailed chemistry of primordial gas. We have also taken into account the numerical "star formation." The following subsections are devoted to describing some details of the scheme.

2.1. Hydrodynamics and Gravity

The hydrodynamics is calculated by the SPH method. We use the version of SPH by Umemura (1993), with the modifications according to Steinmetz & Müller (1993), and we also adopt the particle resizing formalism by Thacker et al. (2000). The gravitational force is calculated by a special-purpose processor for gravity calculation, GRAPE (Sugimoto et al. 1990), which can also accelerate an SPH scheme (Umemura et al. 1993). Here we used the latest version, GRAPE-6 (Makino 2002), which has a speed of 1 Tflops. Eight GRAPE-6 boards are combined with CP-PACS, which is a massively parallel supercomputer at the University of Tsukuba

composed of 2048 processing units (PUs), with a theoretical peak speed of 614 Gflops (Iwasaki 1998). This system is called the Heterogeneous Multicomputer System (HMCS; Boku et al. 2002). The hydrodynamics, radiative transfer, and chemical reactions are solved with CP-PACS. The software originally developed for HMCS can be easily applied to any massively parallel computer connected through TCP-IP with GRAPE-6 boards. Actually, we also used an alpha cluster and a PC cluster instead of CP-PACS as the host.

The softening length for gravity is taken as 60 pc for all SPH and CDM particles. In addition, a minimum size for an SPH particle is introduced so as to prevent the simulation from stopping owing to very short local timescales. We have tested this scheme by the standard Sod's shock tube and Evrard's collapse problems, and the results well reproduce the known solutions.

2.2. Thermal Processes

The nonequilibrium chemistry and radiative cooling for primordial gas are calculated by the code developed by Susa & Kitayama (2000), in which H_2 cooling and reaction rates are taken from Galli & Palla (1998). The H_2 cooling rate induced by collisions with H atoms is plotted in Figure 1 for high-(10^6 cm^{-3}) and low-density (0.1 cm^{-3}) cases. The cooling functions by Hollenbach & McKee (1979) and Lepp & Shull (1983) are also plotted for reference. They agree with each other at the high-density limit (i.e., LTE), whereas they disagree significantly with each other at the low-density limit. We also assessed the contribution of metallic cooling and compared it to H_2 and Lyα cooling in Figure 2 for temperatures below 10^4 K. The cooling rate by metals is evaluated by the fitting formula in Dalgarno & McCray (1972), assuming that the relative abundance of the heavy
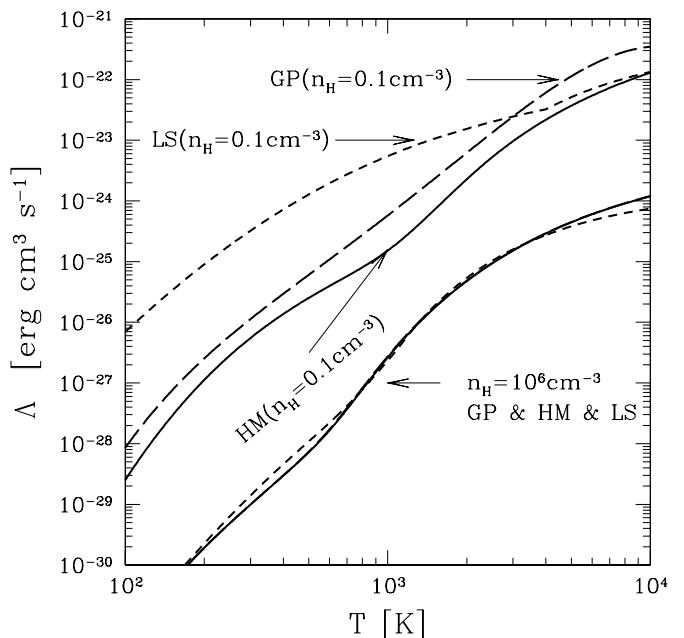

Fig. 1.—H_2 cooling functions induced by H-H_2 collision vs. temperature for two different densities. Solid curves are based on the formula given by Hollenbach & McKee (1979), long-dashed curves on that by Galli & Palla (1998), and short-dashed curves on that by Lepp & Shull (1983). They are discrepant at low density. In this paper, those by Galli & Palla (1998) are adopted.
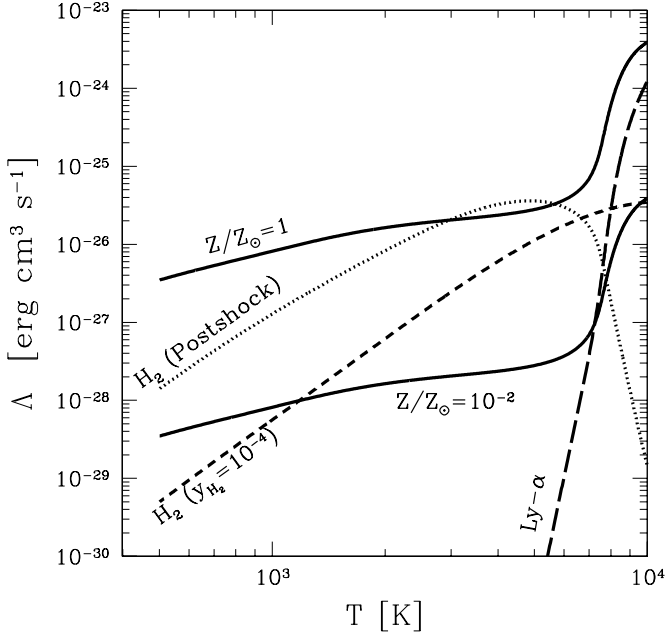
Fig. 2.—Cooling functions below 10^4 K. The two solid lines denote the cooling rate due to metals, assuming $Z/Z_\odot = 1$ and 10^{-2}. The H_2 cooling function is plotted for the postshock region with shock velocity larger than 30 km s^{-1} (*dotted line*) and also for a given abundance of $y_{H_2} = 10^{-4}$ (*short-dashed line*). A long-dashed line represents the rate by hydrogen Lyα.

elements is the same as in the solar neighborhood. The fractions of electrons and H_2 are assumed to be the values behind a shock with a velocity of $v_s > 30$ km s^{-1}, since the initially ionized gas traces a path similar to that of gas behind such a shock (Kang & Shapiro 1992; Corbelli et al. 1997; Susa & Umemura 2000a). We also plot the H_2 cooling function, assuming an H_2 fraction of 10^{-4}, which is favored for clouds with virial temperatures of 10^3 K $\lesssim T_{vir} \lesssim 10^4$ K (Nishi & Susa 1999).[1] As shown in Figure 2, for $T \lesssim 8 \times 10^3$ K, the dominant cooling mechanism is dependent on the metallicity.

In nearby dwarf galaxies, the metal cooling is likely to be important, because the observed metallicity is $Z/Z_\odot \sim 10^{-2}$ to 10^{-1}. On the other hand, observations of Lyα absorption systems at high redshifts imply that the metallicity of the high-z IGM is at a level of $Z/Z_\odot \sim 10^{-2}$ to 10^{-3} (Songaila 2001). Hence, the cooling rate by metals is rather smaller than that by H_2, as long as 10^3 K $\lesssim T \lesssim 10^4$ K. In the present paper, we focus on the primary star-forming phase in dwarf galaxies from metal-poor gas with the metallicity seen in the IGM or more primordial gas. If one pursues the subsequent recycling phase of the interstellar medium with supernova (SN) explosions, it is definitely requisite to include the metal cooling. Such a recycling effect is important for the chemical evolution of galaxies, but the issue is beyond the scope of present paper and left to future study.

It should also be noted that the effects by metals can play a significant role even at a level of $Z/Z_\odot \sim 10^{-5}$ for the runaway collapse onto a primordial protostar (Omukai 2000; Bromm et al. 2001; Schneider et al. 2002), although here we

do not pursue the runaway to a star in such dense, cold regions. Based on these arguments, we neglect the cooling by metals in this paper, and the thermal processes are calculated with the chemistry for primordial abundance gas.

2.3. Radiative Transfer

The photoionization and the photoheating rates are given, respectively, by

$$k_{ion} = n_{H\,I} \int_{\nu_L}^{\infty} \int \frac{I_\nu(s)}{h\nu} \sigma_\nu \, d\Omega \, d\nu, \tag{1}$$

$$\Gamma_{ion} = n_{H\,I} \int_{\nu_L}^{\infty} \int \frac{I_\nu(s)}{h\nu} \sigma_\nu (h\nu - h\nu_L) \, d\Omega \, d\nu. \tag{2}$$

Here $n_{H\,I}$ represents the number density of neutral hydrogen, σ_ν is the photoionization cross section, ν_L is the frequency at the Lyman limit, Ω is the solid angle, and $I_\nu(s)$ is the intensity of the UV radiation, with s denoting the distance from the source of ionizing photons. The value of $I_\nu(s)$ is determined by solving the radiative transfer equation,

$$\frac{dI_\nu}{ds} = -n_{H\,I}\sigma_\nu I_\nu, \tag{3}$$

where the reemission term is not included, because we employ an on-the-spot approximation. The transfer equation (3) is solved based on the method developed by Kessel-Deynet & Burkert (2000), which utilizes the neighbor lists of SPH particles to assess the optical depth from a certain source to an SPH particle. Here we assume a single point source, located very far from the simulated region, and control the UV intensity by specifying the incident flux to the simulation box, as described in § 2.5. It is noted that the irradiation from one side can overestimate the effects of shadowing, and internal sources, if they form, might also play a significant role (Ricotti et al. 2002a, 2002b). On the other hand, in Kessel-Deynet & Burkert's method, the numerical diffusion of radiation is not negligible. This effect tends to reduce the shadowing effect. These points should be improved on in the future.

We parallelize the scheme so that we can implement it on massively parallel computer systems, such as CP-PACS. For the purpose, particles should be classified into subsets, which are assigned to the PUs. The domain decomposition is performed as shown in Figure 3. The first step is to project the particle positions onto the plane that is perpendicular to the light rays of the external single source. Since the position of the source is assumed to be far away from the simulated region, we can approximate the light rays to be parallel. The second step is to sort the projected positions of the particles on the x-y plane. Then, with the results of coordinate sorting, we generate subsets with equal numbers of particles, which are assigned to computational domains, i.e., PUs. In the Appendix, a test calculation using this scheme is presented for the propagation of the ionization front in a uniform medium. We remark that the present parallelization scheme is not valid for multiple sources, because the domain decomposition is based on the projection of all particles onto the plane perpendicular to the source direction. Hence, it is necessary
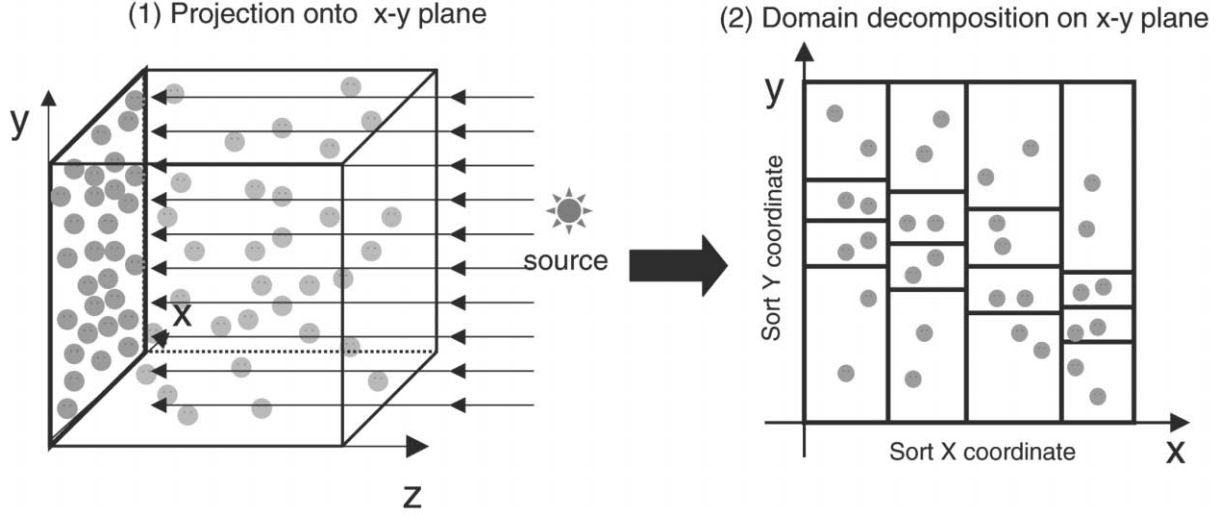
---

[1] In this case, the fraction of electrons can be an order of magnitude smaller than in the high-velocity postshock cases. Hence, the cooling rate by metals becomes an order of magnitude smaller, since the cooling is induced by collisions between electrons and heavy elements.

to invoke a new technique in order to include internal sources in the future analysis.

Combining equations (1)–(3), we can rewrite the ionization and photoheating rates as follows:

$$k_{\mathrm{ion}} = -\frac{d}{ds} \int_{\nu_L}^{\infty} \int \frac{I_\nu(s)}{h\nu} \, d\Omega \, d\nu$$

$$= -\frac{d}{ds} \int_{\nu_L}^{\infty} \frac{F_\nu(s)}{h\nu} \, d\nu, \qquad (4)$$

$$\Gamma_{\mathrm{ion}} = -\frac{d}{ds} \int_{\nu_L}^{\infty} \int \frac{I_\nu(s)}{h\nu} (h\nu - h\nu_L) \, d\Omega \, d\nu$$

$$= -\frac{d}{ds} \int_{\nu_L}^{\infty} \frac{F_\nu(s)}{h\nu} (h\nu - h\nu_L) \, d\nu. \qquad (5)$$

When we need to assess the rates at each grid point (or each SPH particle), we use the following formula:

$$k_{\mathrm{ion}}\left(i + \frac{1}{2}\right) = \frac{1}{s_{i+1} - s_i} [\Phi_1(i) - \Phi_1(i+1)], \qquad (6)$$

$$\Gamma_{\mathrm{ion}}\left(i + \frac{1}{2}\right) = \frac{1}{s_{i+1} - s_i} [\Phi_2(i) - \Phi_2(i+1)], \qquad (7)$$

where

$$\Phi_1(s) = \int_{\nu_L}^{\infty} \frac{F_\nu(s)}{h\nu} \, d\nu, \qquad (8)$$

$$\Phi_2(s) = \int_{\nu_L}^{\infty} \frac{F_\nu(s)}{h\nu} (h\nu - h\nu_L) \, d\nu. \qquad (9)$$

Here $i + \frac{1}{2}$ denotes the grid point at which the rates are assessed, and i denotes the boundary between the $i - \frac{1}{2}$ and $i + \frac{1}{2}$ grids. In the present simulation, these grids are generated by the method in Kessel-Deynet & Burkert (2000). The above formula has the important advantage that the propagation of

the ionization front is properly traced even for a large grid size with optical depth greater than unity ($\tau > 1$) (Kessel-Deynet & Burkert 2000; Abel, Norman & Madau 1999).

2.4. *Star Formation Algorithm*

Here the "star formation" algorithm used in this simulation is described. At each time step, we pick up the SPH particles that satisfy the following four conditions: (1) div $v < 0$, (2) $\rho/\bar{\rho} > 200$, (3) $T < 5 \times 10^3$ K, and (4) $y_{H_2} > 5 \times 10^{-4}$. These conditions look similar to those adopted by Cen & Ostriker (1993), but conditions 3 and 4 are different. The first condition guarantees that the gas surrounding the particle is infalling. In addition, if the region is virialized, the density around the particle should satisfy the second condition. Conditions 3 and 4 cannot be satisfied unless the region is self-shielded against the UVB and thereby H_2 cooling is effective. These two conditions are essential for star formation, although they are not taken into account in previous simulations. In addition, conditions 3 and 4 match the observations of the H I contents in nearby dwarf galaxies, which indicate that the presence of cold ($T \sim 10^3$ K) H I gas is a good indicator of star formation activities (Young & Lo 1997a, 1997b).

The next step is to define the timescale of "star formation." In order to define the conversion timescale from gas to stars, we use the following simple and often-used formula:

$$\frac{d\rho}{dt} = -\frac{d\rho_{\mathrm{star}}}{dt}, \qquad (10)$$

$$\frac{d\rho_{\mathrm{star}}}{dt} = \frac{c_* \rho}{t_{\mathrm{ff}}}, \qquad (11)$$

where t_{ff} is the local free-fall timescale, ρ_{star} is the mass density of star particles, and c_* denotes the parameter of star formation timescale. Following the above expression, an SPH particle that satisfies the conditions for star formation is converted to a collisionless particle after $\Delta t = t_{\mathrm{ff}}/c_*$. Here we use $c_* = 0.1$ for the fiducial model, and we also investigate $c_* = 1$ and $c_* = 0.01$ for several cases. In previous numerical simulations on the formation of disk galaxies, c_* is sometimes

set to be 0.05–0.1, applying the cooling criterion of 10^4 K, in order to regulate both the star formation efficiency and the star formation rate (SFR) to match Kennicutt's law (e.g., Kennicutt 1998; Koda, Sofue, & Wada 2000). However, in the present simulation, the star formation efficiency is physically regulated in terms of temperature criterion 3. Hence, in this paper, $c_* = 1$ does not mean that all the gas cooled to 10^4 K is converted into stars. Here c_* just controls the star formation timescale or SFR.

2.5. Setup

The initial particle distributions in a CDM-dominated universe are generated by a public domain code, GRAFIC, which is a part of COSMICS. Throughout this paper, we assume a Λ-dominated flat universe, with $\Omega_M = 0.3$, $\Omega_\Lambda = 0.7$, $\Omega_B h^2 = 0.02$, and $h = 0.7$. The total mass of the simulated region is 10^8–$10^9\ M_\odot$, in which a halo collapses at $1 \lesssim z_c \lesssim 10$. We first generate the positions and velocities of particles in a cube, with the constraint that the peak of an overdense region is located at the center of the cube. The peak height is controlled so that the overdense region collapses at a given epoch. Then we hollow out a spherical region from the cube, so that the sphere contains the overdense region and the radius of the sphere agrees with the smoothing scale of the overdensity. Then we attach a rigidly rotating velocity field to the spherical region that corresponds to spin parameter $\lambda = 0.05$ (Heavens & Peacock 1988; Steinmetz & Bartelmann 1995). In each run, we define the halo mass $M_{\rm halo}(z)$ as the mass within the radius $R_{\rm vir}(z)$. The virial radius $R_{\rm vir}(z)$ is defined by the condition

$$\bar{\rho}_{\rm DM}[< R_{\rm vir}(z)] = 18\pi^2 \rho_0 (1+z)^3, \qquad (12)$$

where $\bar{\rho}_{\rm DM}(< R)$ is the averaged dark matter density within the radius R measured from the center of mass of the whole system. The quantity ρ_0 denotes the averaged density of the present universe. We also define the collapse epoch z_c as the epoch by which a half of the dark halo mass collapses within the radius $R_{\rm vir}(z)$. The typical halo mass just after the virialization is approximately 60% of the total mass of the simulated region. These are tabulated in Table 1.

For the largest simulations, 2^{17} (131,072) SPH particles and 2^{17} dark matter particles are employed. In addition, a case study is done for all parameters with a smaller number of particles, 2^{15} SPH particles and 2^{15} dark matter particles. Finally, we give the Hubble expansion velocity to all particles, in addition to the already generated peculiar velocity fields.

We also fix the initial abundance of chemical species. We have taken the values of the canonical model in Galli & Palla (1998). The evolution of the UVB is modeled as follows. The spectrum shape of the UVB is assumed to be $I_\nu \propto \nu^{-1}$, and the intensity I_{21}, which is the UVB intensity normalized by 10^{-21} ergs s^{-1} cm^{-2} sr^{-1} Hz^{-1}, is assumed to be $I_{21} = [(1+z)/3]^3$ for $z \leq 2$ and $I_{21} = 1$ for $2 < z \leq 4$. This dependence is consistent with the UV intensity in the present epoch (Maloney 1993; Dove & Shull 1994) and the value inferred from the QSO proximity effects at high redshifts (Bajtlik, Duncan, & Ostriker 1988; Giallongo et al. 1996), although there is an uncertainty of $10^{\pm 0.5}$ at $2 < z \leq 4$. As for higher redshift epochs, we employ two regimes. One is a regime with $z_{\rm reion} \approx 7$, which is provided by $I_{21} = \exp[3(4-z)]$ for $z > 4$ (Umemura et al. 2001). Such a UVB evolution is suggested by a comparison between Lyα continuum depression in high-z QSO spectra and the simulations of QSO absorption lines based on six-dimensional radiation transfer calculations on the reionization (Nakamoto et al. 2001). In this regime, the reionization proceeds from $z \approx 9$ and is completed at $z \approx 7$. Most of the runs are performed in this regime. However, for comparison, we also investigate a high-z reionization regime ($z_{\rm reion} \approx 17$), such as has recently been inferred by the *WMAP* (Kogut et al. 2003). In this regime, the intensity of the UVB is modeled by $I_{21} = \max \{\exp[3(4-z)],\ 0.01\}$ for $4 < z < 17$ and $I_{21} = \exp[3(17-z)]$ for $z > 17$, based on Nakamoto et al. (2001). We calculate two typical runs in the high-z reionization model.

3. RESULTS

In Table 1, the model parameters studied here and the basic results are summarized, where z_c is the collapse redshift, $M_{\rm halo}$ is the halo mass, $T_{\rm vir}$ is the virial temperature, $\sigma_{\rm 1D}$ is the line-of-sight velocity dispersion of the stellar component, and $\sigma_{\rm 1D}$ (DM) is that of the dark matter component. These values should be defined as functions of redshift, but the tabulated values are assessed just after the virialization. The effective radius of the formed galaxy is $R_{\rm half}$, $f_{\rm star}$ is the final stellar fraction, and $M_{\rm halo}/L$ is the mass-to-luminosity ratio in solar units. We show the detailed results in the following subsections.

3.1. Reionization Feedback

Figures 4 and 5 show two typical results, where $c_* = 0.1$ for both cases. Figure 4 shows the low-z_c ($z_c \simeq 1.7$) and less massive case ($M_{\rm halo} \simeq 6 \times 10^7\ M_\odot$). Dots in the figure denote the location of SPH particles and numerically formed stars.

TABLE 1

Properties of Formed Galaxies

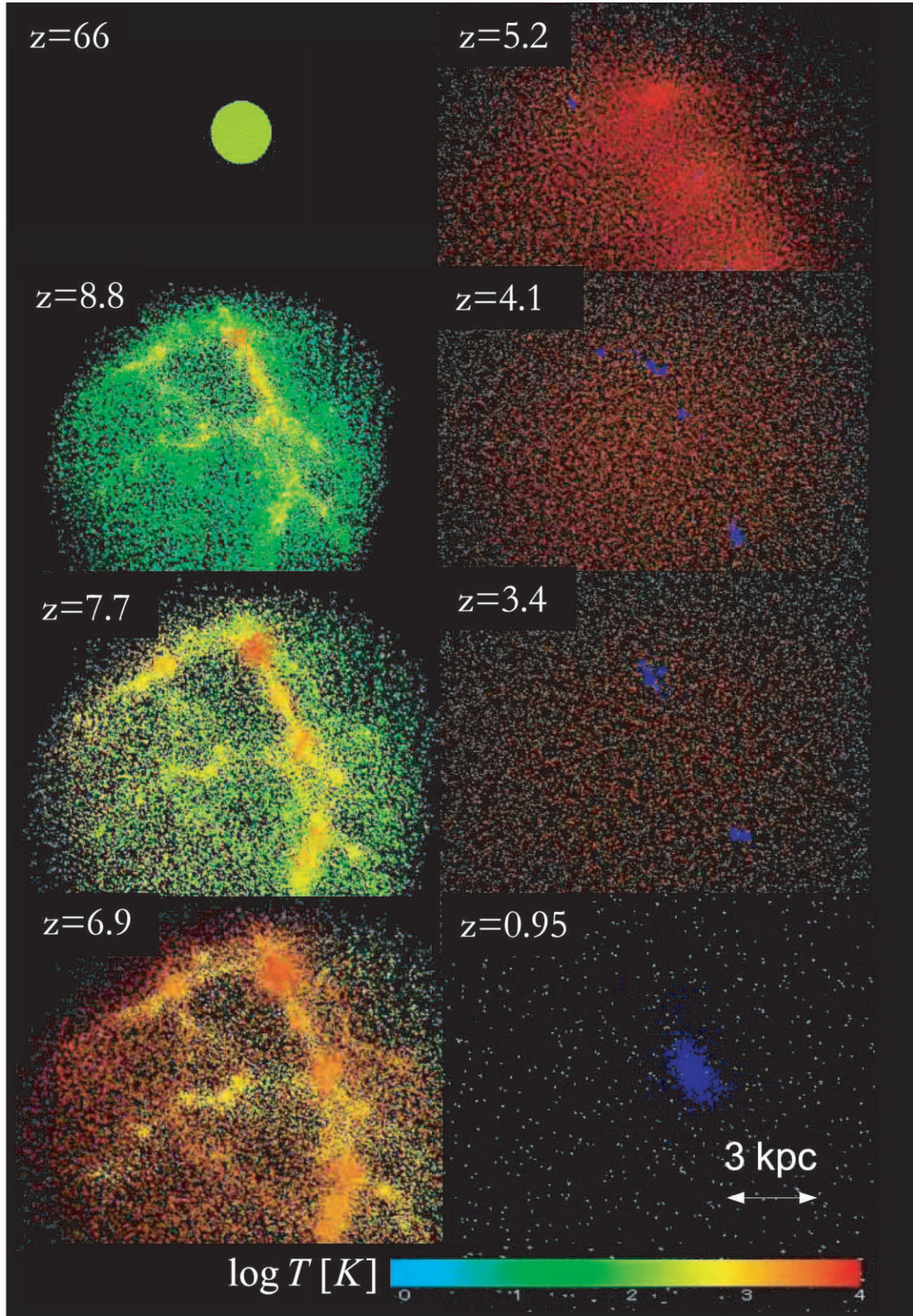| z_c	$M_{\rm halo}$ ($M_\odot$)	$T_{\rm vir}$ (K)	$\sigma_{\rm 1D}$ (km s^{-1})	$\sigma_{\rm 1D}$(DM) (km s^{-1})	$R_{\rm half}$ (pc)	$f_{\rm star}$	$M_{\rm halo}/L$
1.7.....	5.9×10^7	3.6×10^3	4.6	5.5	62	0.28	63
3.4.....	5.9×10^7	5.1×10^3	5.1	6.5	58	0.37	50
5.1.....	6.1×10^7	6.3×10^3	5.7	7.2	69	0.47	44
6.5.....	6.1×10^7	8.2×10^3	6.4	8.2	66	0.61	36
8.1.....	6.1×10^7	1.0×10^4	7.1	9.2	62	0.71	33
1.1.....	6.0×10^8	1.7×10^4	14	12	2.9×10^2	0.43	40
2.9.....	6.0×10^8	2.0×10^4	16	14	2.1×10^2	0.55	31
4.5.....	6.0×10^8	2.0×10^4	17	16	2.2×10^2	0.68	31
6.0.....	6.1×10^8	2.1×10^4	19	19	1.8×10^2	0.79	29
7.6.....	6.1×10^8	2.6×10^4	20	21	1.6×10^2	0.93	26

FIG. 4.—Time evolution of the spatial distributions of SPH and star particles for $M_{\mathrm{halo}} \simeq 6 \times 10^7 \ M_\odot$ and $z_c \simeq 1.7$. The figure consists of eight panels. The top left panel shows the distribution of SPH particles at a very early phase; the sequence continues downward in the left column, then resumes in the top right panel. The corresponding redshift is printed at the top left-hand corner of each panel. The colors of the dots represent the logarithmic temperature of the SPH particles, and the color legend is shown at the bottom in a logarithmic scale. The physical scale ruler (3 kpc) is in the bottom right panel. Blue dots do not represent SPH particles but star particles.

z=100 z=5.5

z=29 z=7.1

z=17 z=7.7

z=9.5 z=3.9

3 kpc

$\log T\,[K]$
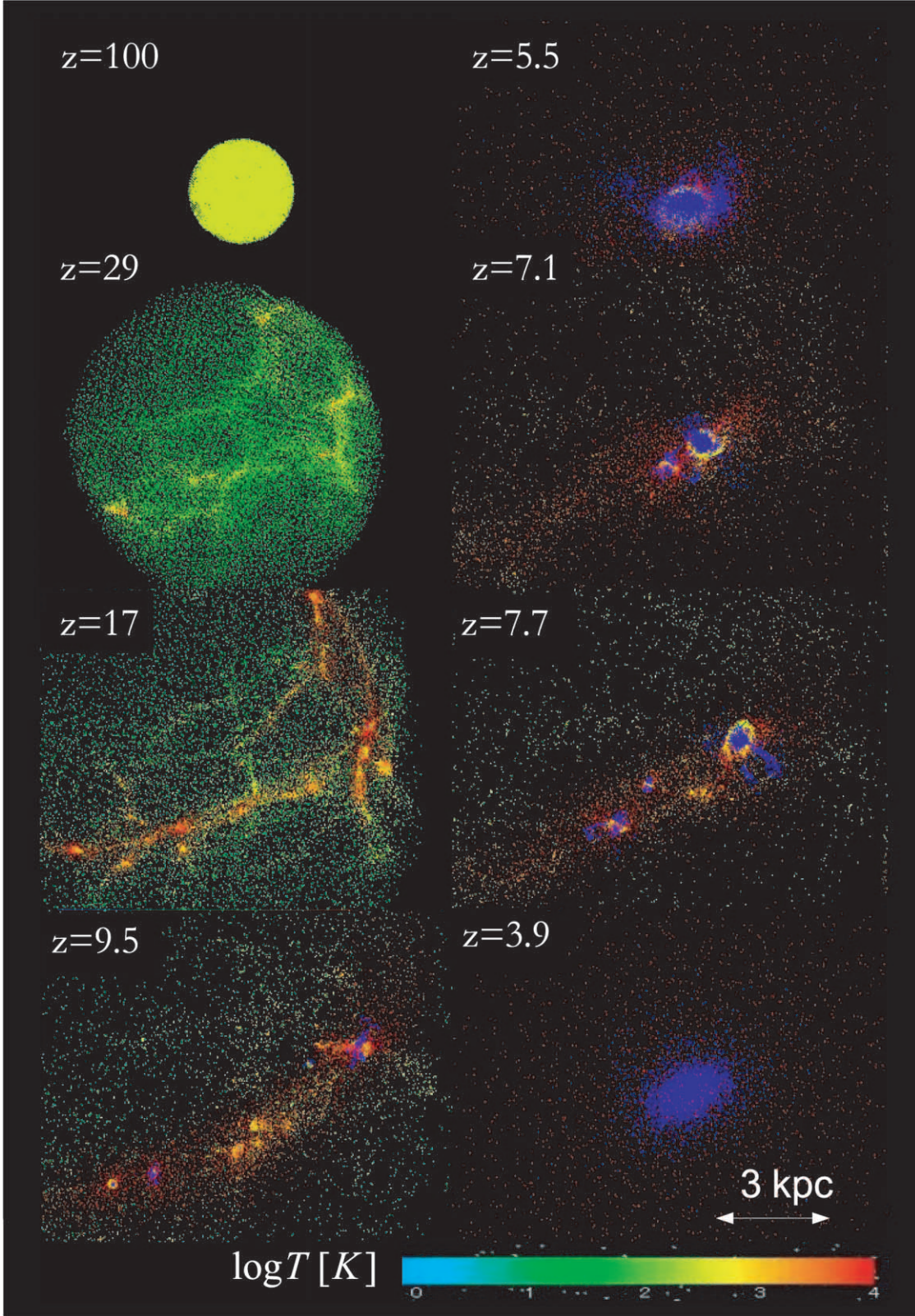
Fig. 5.—Same as Fig. 4, except that the parameters are $M_{\rm halo} \simeq 6 \times 10^8\ M_\odot$ and $z_c \simeq 7.6$

The colors of the particles represent the gas temperature (the color legend is shown at the bottom), except that blue particles denote stars. At $z \simeq 66$ (*first panel*), the initial condition is set in a spherical region, as described in § 2.5. Thereafter, the system expands by the cosmic expansion, and baryon perturbations are also induced by imprinted dark matter fluctuations (*second panel*). At $z \simeq 9$, the first objects with a mass of $\sim 10^6$–$10^7\ M_\odot$ form at density peaks (*second and third panels*). This is consistent with previous results by Tegmark et al. (1997) and Fuller & Couchman (2000). At $z \approx 7$, the

system is reionized overall and reheated by the UVB (*fourth panel*). Then, a portion of the cooled gas that had once settled into the first objects is evaporated as a pressure-driven thermal wind at $z \approx 5$ (*fifth panel*). However, a significant number of baryons are self-shielded against the UVB at high-density peaks even during the reionization, so that photoheating is precluded deep inside the peaks, and eventually stars form there. As a result, small star clusters are left after the reionization epoch (*sixth panel*). The stellar clusters coalesce with each other in a dissipationless fashion, as dark matter fluctuations grow hierarchically (*seventh panel*). Finally, a subgalactic spheroidal system with a high total mass–to–stellar mass ratio ($M_{\mathrm{halo}}/M_{\mathrm{star}} = 20$) forms. If we assume the stellar mass–to–luminosity ratio of 3 in solar units that comes from a Salpeter-like initial mass function, then the mass-to-light ratio of this system is assessed to be $M_{\mathrm{halo}}/L = 63$.

In the above case, baryons are cooled to form stars only at density peaks, and gas in other regions is photoevaporated, resulting in a thermal wind. However, the evolution is quite different for the high-z_c and massive-halo model. Figure 5 represents the $z_c \simeq 7.6$ and $M_{\mathrm{halo}} \simeq 6 \times 10^8 \ M_\odot$ case. In this case, most of baryons collapse before the reionization. As a result, the photoevaporation is less effective than in the low-z_c

case, and thus the whole system does not lose a significant portion of baryonic matter. Finally, a formed spheroidal system has $M_{\mathrm{halo}}/M_{\mathrm{star}} = 7.7$, which is close to the assumed initial total mass–to–baryonic mass ratio, $\Omega/\Omega_B = 7.35$. The mass-to-light ratio of this system is assessed to be $M_{\mathrm{halo}}/L = 26$.

3.2. *Star Formation History*

In Figure 6, the SFHs are shown for four typical runs: low-mass ($6 \times 10^7 \ M_\odot$) cases with $z_c = 1.7$ and 8.1 and high-mass ($6 \times 10^8 \ M_\odot$) cases with $z_c = 1.1$ and 7.6. As commonly seen, the SFR peaks before 10^9 yr ($z \gtrsim 5$), and the star formation activity is substantially suppressed by the UVB after the reionization, $z \lesssim 5$. This indicates that the star formation mainly occurs in high-density regions that collapsed prior to the reionization. The peak SFR is lower in the systems with lower collapsing epochs. However, the difference is not very drastic. The peak SFR in $z_c \approx 1$ cases is roughly half of that in $z_c \approx 8$ cases. Based on the criterion for spherical clouds (e.g., Kitayama et al. 2001), the clouds should be completely photoevaporated in the two cases with $z_c \approx 1$. However, the present results show that high-density peaks that collapse before the reionization contribute significantly to star
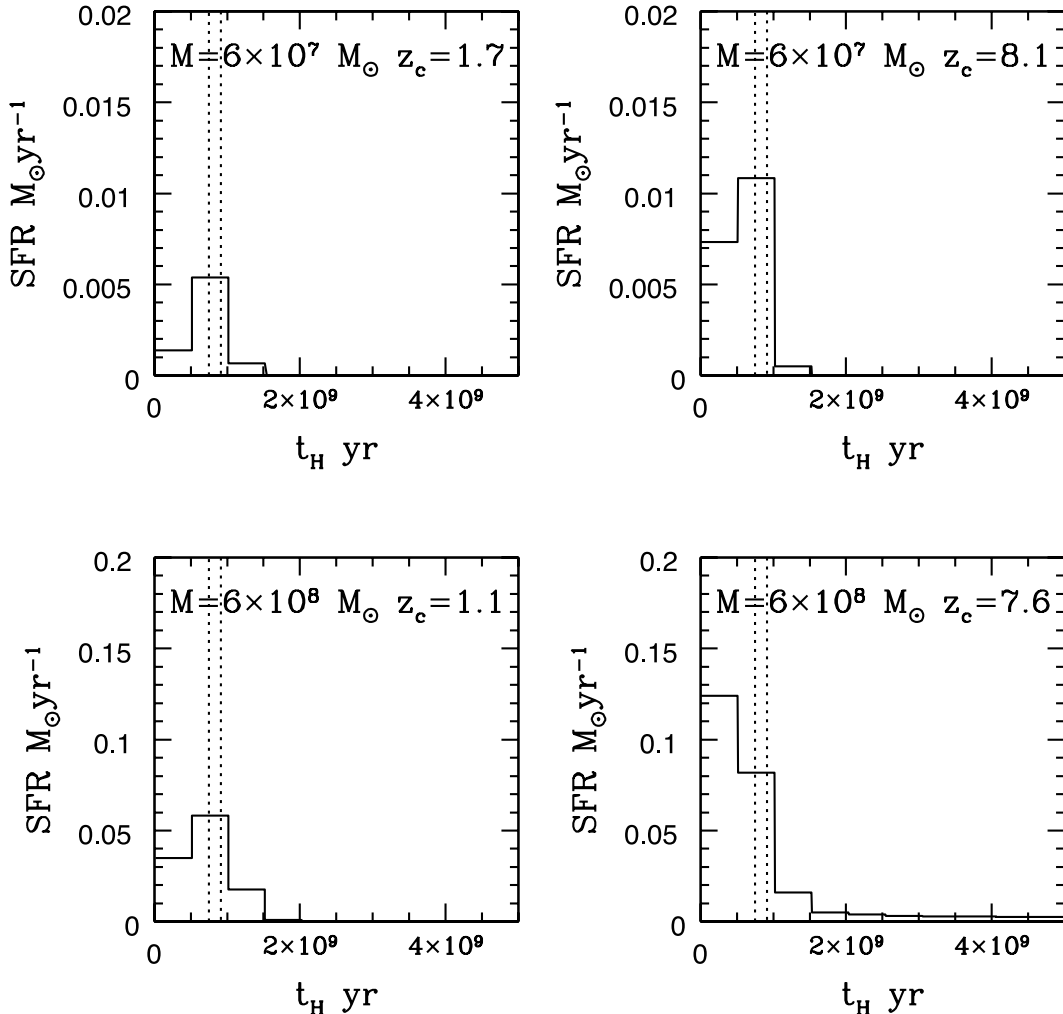

FIG. 6.—Time variation of the SFR vs. cosmic time. Panels represent the results of four different runs, with the parameters displayed in each panel. The vertical dashed lines denote $z = 7$ and 6, between which the reionization is almost completed in this model.

formation even in such low-z_c objects. This is a consequence of the hierarchical growth of density fluctuations that is caused by the CDM spectrum.

As another important result, it should be noted that the star formation activity in the case with $M_{halo} \simeq 6 \times 10^8 \ M_\odot$ for high z_c continues even after the reionization. This is caused by the depth of the gravitational potential. A massive galaxy with high z_c has a deeper gravitational potential. Thus, the dark halo can prevent the photoheated gas from blowing out into intergalactic space. Instead, the heated gas slowly accretes in the potential of the dark halo. Eventually, the gas is self-shielded from the UVB and cools by H_2, so that stars form even in the UVB.

In Figure 7, the final fraction of stars, f_{star}, is plotted against the collapse epoch z_c, where f_{star} is defined by the total mass of star particles divided by the total baryonic mass at $z = 1$ ($f_{star} \equiv M_{star}/M_{baryon}$). The five-pointed stars represent the results of $M_{halo} \simeq 6 \times 10^8 \ M_\odot$ runs, and the pentagons denote those of $M_{halo} \simeq 6 \times 10^7 \ M_\odot$ runs, where c_* is assumed to be 0.1. The stellar fraction is smaller for $M_{halo} \simeq 6 \times 10^7 \ M_\odot$ cases than for $M_{halo} \simeq 6 \times 10^8 \ M_\odot$ cases. This comes from the SFH shown above. The massive objects tend to retain more gas components than less massive objects in the presence of the UVB.

In addition, f_{star} decreases monotonically with decreasing z_c for both the $M_{halo} \simeq 6 \times 10^8 \ M_\odot$ and $M_{halo} \simeq 6 \times 10^7 \ M_\odot$ cases. It is found that the dependence of f_{star} on $1 + z_c$ is almost linear, and its relation is given by

$$f_{star} \simeq a(M)(1 + z_c) + b(M), \tag{13}$$

where $a(6 \times 10^8 \ M_\odot) = 7.7 \times 10^{-2}$, $a(6 \times 10^7 \ M_\odot) = 6.9 \times 10^{-2}$, $b(6 \times 10^8 \ M_\odot) = 0.26$, and $b(6 \times 10^7 \ M_\odot) = 7.7 \times 10^{-2}$. We emphasize that even for galaxies assembled after the reionization, some fraction of baryons are cooled and form stars at high-density peaks. The two vertical lines in Figure 7 denote the critical redshifts, obtained by Kitayama et al. (2001), after which protogalactic clouds are photoevaporated. The condition for $M_{halo} \simeq 6 \times 10^7 \ M_\odot$ is denoted by a solid line and that for $M_{halo} \simeq 6 \times 10^8 \ M_\odot$ by a dotted line. This result shows again that the inhomogeneity in protogalactic clouds is crucial for the star formation in them, because a portion of the baryons collapse and cool before the reionization and also because some fraction of gas is self-shielded from the UVB even after the reionization if the gas accretes in the dark matter potential.

In Figure 7, we also plot the results with $c_* = 1$ (high-SFR runs) and $c_* = 0.01$ (low-SFR runs). As seen clearly, the results are basically the same as in the case of $c_* = 0.1$. This is physically understood as follows: In the present simulations, stars form from overdense regions with $\rho \gtrsim 10^{-22} \ g \ cm^{-3}$. Then, the star formation timescale assessed by the present star formation algorithm (eq. [11]) is given by $t_{SF} = t_{ff}/c_* \lesssim 10^7 c_*^{-1} \ yr$. On the other hand, the UV feedback is quite effective at $z \lesssim 5$, when the age of the universe is greater than $10^9 \ yr$. Thus, the main episode of the initial star formation ends before the reionization as long as $c_* > 0.01$. Moreover, the density of star-forming regions is higher if c_* is smaller, because further radiative cooling works before the gas is converted to stars. Therefore, the local free-fall time of the star-forming region is shorter for smaller c_*. Consequently, c_* is not as important in determining the final stellar fraction. However, if we adopt $c_* = 0.01$, the SFH is modified as a
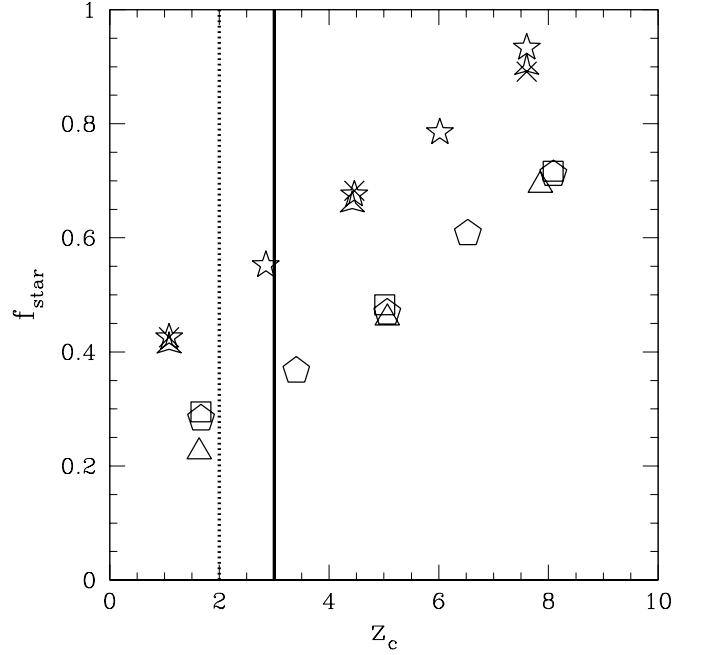

Fig. 7.—Final stellar fraction f_{star} vs. collapse redshift. Each symbol denotes the result of a run: pentagons ($c_* = 1$), squares ($c_* = 0.1$), and triangles ($c_* = 0.01$) denote the runs with $M_{halo} \simeq 6 \times 10^7 \ M_\odot$. Similarly, five-pointed stars ($c_* = 1$), crosses ($c_* = 0.1$), and three-pointed stars ($c_* = 0.01$) represent the results for relatively massive galaxies ($M_{halo} \simeq 6 \times 10^8 \ M_\odot$).

matter of course. The epoch of star formation is shifted to a later epoch for $c_* = 0.01$, as shown in Figure 8. Especially in cases with high mass and high-z_c, the star formation activity after the reionization is enhanced compared to the $c_* = 0.1$ case. The relation of this result to the continuous SFH inferred in nearby dwarf galaxies (e.g., Mateo 1998) will be discussed in § 4.2.

3.3. Radiative Transfer Effect

Here we show more specifically the effects of radiative transfer in the present simulations. For comparison, we perform control runs, in which gas is assumed to be optically thin against UV radiation. In Figure 9, the time variations of stellar fractions are compared between the runs with and without radiative transfer. The parameters are the same as those in Figure 6. For all runs, it is clear that star formation activities are suppressed at earlier epochs and thoroughly terminated after the reionization in optically thin simulations. In Figure 10, the final stellar fractions (f_{star}) are shown for the runs with and without radiative transfer. The optically thin approximation underestimates the stellar fraction by a factor of 1.5–2 for all runs in the $z_{reion} \simeq 7$ models, regardless of the mass and collapse epoch. The radiative transfer effect is even more crucial in $z_{reion} \simeq 17$ models, as shown in § 3.5. The reduction of f_{star} by dismissing the radiative transfer is more than an order of magnitude if $z_{reion} \simeq 17$. Hence, it is clear that the self-shielding does work to form stars effectively during the reionization.

In addition, in the bottom right-hand panel of Figure 9, where $M_{halo} \simeq 6 \times 10^8 \ M_\odot$ and $z_c = 7.6$, f_{star} continues to increase if the radiative transfer is incorporated. Since the gravitational potential is deep enough to sustain the photo-heated gas in this case, some gas is self-shielded in the course
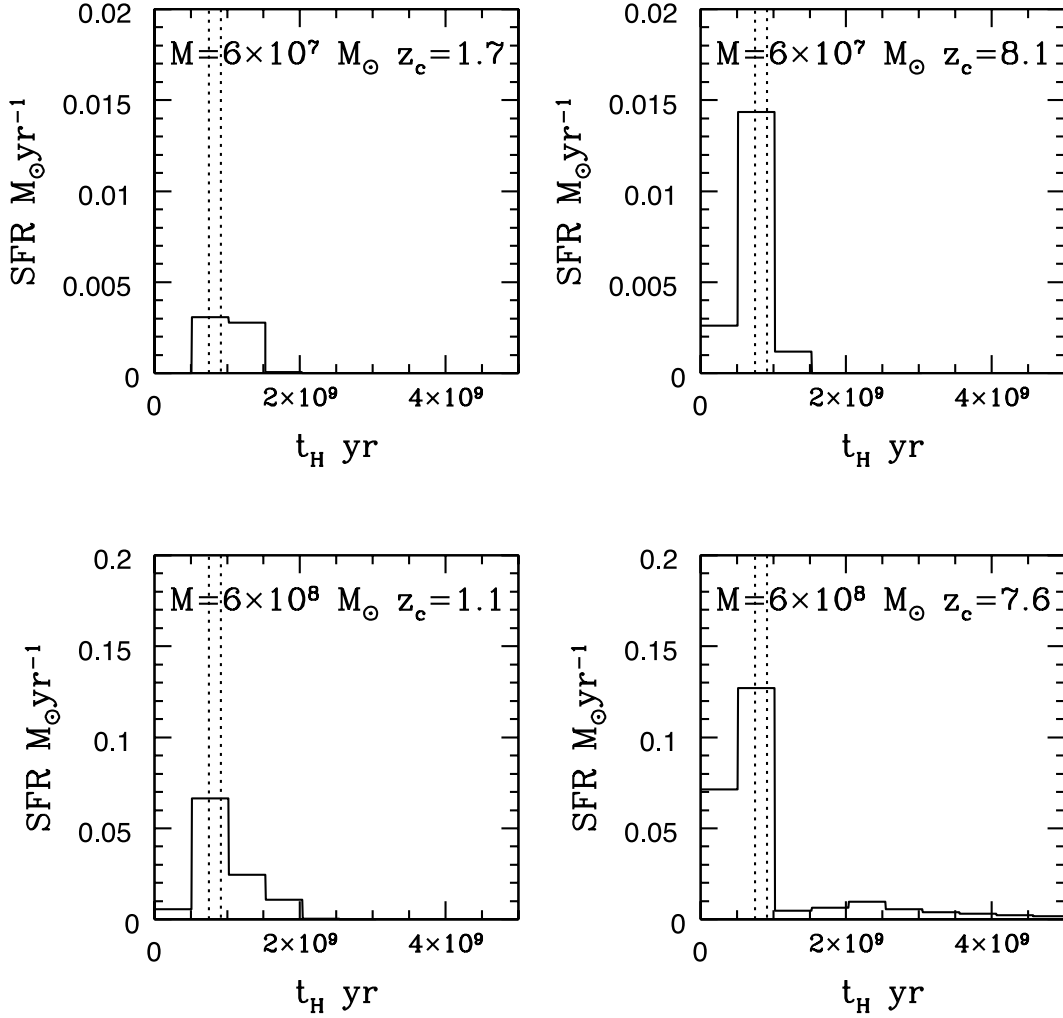
FIG. 8.—Same as Fig. 6, except that $c_* = 0.01$

of accretion onto local density peaks, so that stars continue to form. In the optically thin simulation, the accreted gas cannot be cooled below 10^4 K, owing to the absence of the shielding effect, so no stars form after the reionization.

3.4. Kinematic Properties

In Table 1, the one-dimensional velocity dispersion of the formed stars (σ_{1D}) and effective size R_{half} of the resultant spheroidal system are listed for various runs. Here the effective size, R_{half}, is defined so that half of the stars are contained within the radius. In the low-z_c case shown in Figure 4, gas can cool at density peaks before the reionization and form compact star clusters. The star clusters coalesce in a dissipationless fashion to form a single spheroidal system eventually. On the other hand, in the high-z_c case shown in Figure 5, the formation process of the final stellar system is rather different, because the star formation proceeds not only at the density peaks but also after the collapse of the whole system, which takes place after the reionization. In order to clarify the difference quantitatively, we plot the time variation of the ratio of the total kinetic energy from random motion (E_{ran}) to the total rotational energy (E_{rot}). Here E_{rot} is defined as the summation of the rotational energy of baryonic particles (i.e., SPH particles and star particles) that are contained in a sphere with a radius of $R_{vir}(z)$ from the center of gravity:

$$E_{rot} = \sum_{r_i < R_{vir}(z)} \frac{1}{2} m_i v_{rot,i}^2, \qquad (14)$$

where $v_{rot,i}$ is the angular velocity of ith particle. The quantity E_{ran} is defined as the rest of the kinetic energy; that is, $E_{ran} = E_{kin} - E_{rot}$, where E_{kin} is the total kinetic energy. When the velocity field is isotropic, the ratio E_{rot}/E_{ran} should be $\frac{1}{5}$, according to the present definition. Figure 11 shows the time evolution of the ratio E_{rot}/E_{ran} for four typical runs after the collapse epoch. As shown in this figure, E_{rot}/E_{ran} is well below unity for all cases after z_c. This means that these systems are not rotationally supported. However, if we take a closer look, the ratio for the high-mass and high-z_c case ($M_{halo} \simeq 6 \times 10^8 \, M_\odot$, $z_c \simeq 7.6$) is somewhat larger than the others. This reflects the fact that part of the gas forms a rotating disk before it is converted into stars. On the other hand, for the other cases, gas is lost after the reionization era ($z \lesssim 7$), and no rotating disk forms.

3.5. Effects of Early Reionization

Here we attempt to evaluate the effects of early reionization, as inferred by the results of WMAP (Kogut et al. 2003). We perform two runs in the high-z reionization regime ($z_{reion} \approx 17$) described at the end of § 2.5. Both runs are high-z_c models,
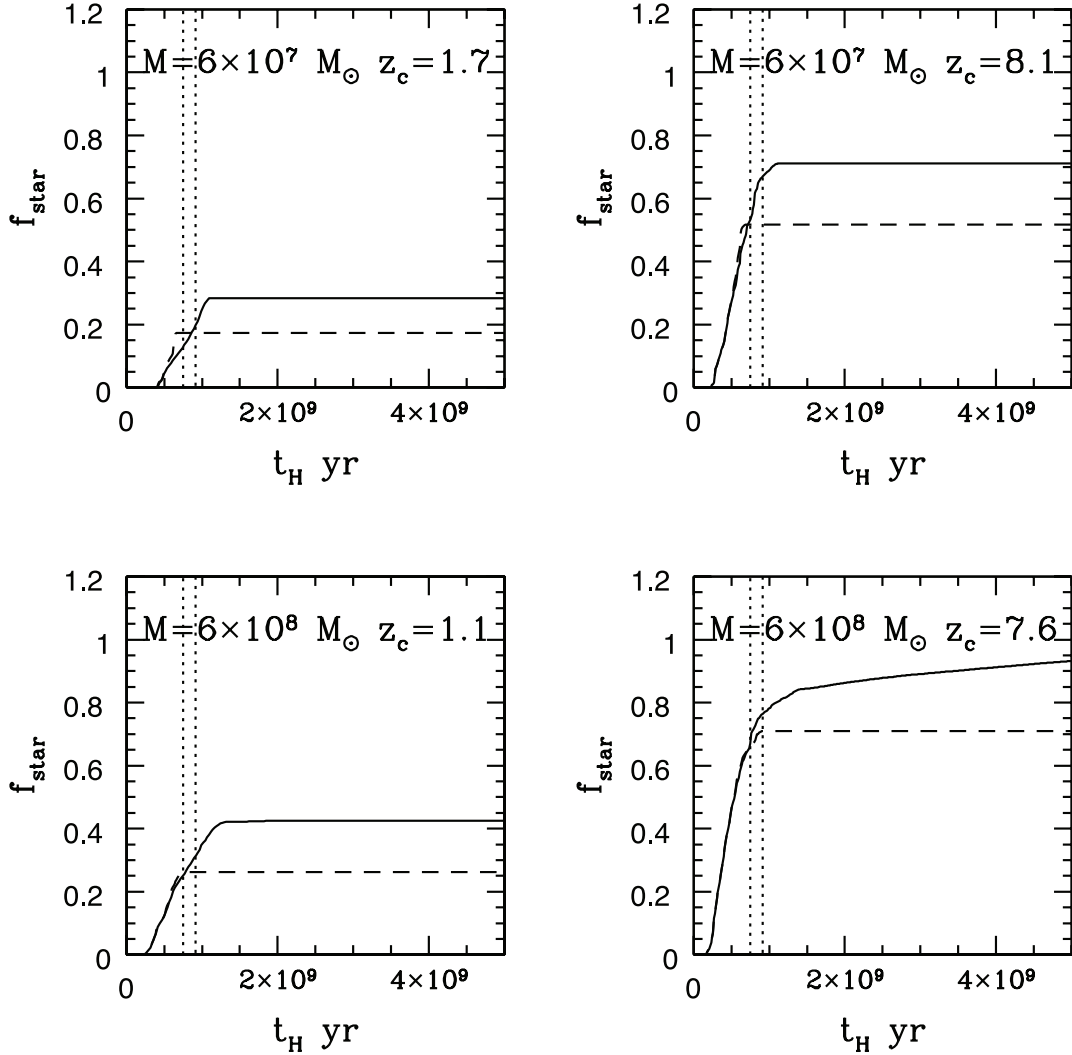
Fig. 9.—Time variations of stellar fraction f_{star} vs. cosmic time for transfer and optically thin cases. Solid lines show the results with radiative transfer, while dashed lines show those under the optically thin assumption. Parameters for the panels are the same as in Fig. 6. The vertical dashed lines denote $z = 7$ and 6, between which the reionization is almost completed in this model.

in which $M_{halo} \simeq 6 \times 10^7 \ M_\odot$ with $z_c = 8.1$ or $M_{halo} \simeq 6 \times 10^8 \ M_\odot$ with $z_c = 7.6$. The SFH and the time evolution of stellar fractions are shown in Figure 12. First, for the former run ($M_{halo} \simeq 6 \times 10^7 \ M_\odot$), the effects of early reionization feedback are noticeable, and the fraction of the stellar component becomes roughly 4 times smaller than in the fiducial reionization regime ($z_{reion} \approx 7$). Nonetheless, some fraction of baryons are cooled to form stars even at $z < 17$, owing to the effects of self-shielding. This is partly because the IGM is not perfectly transparent to the UVB, even if the UV intensity is strong enough to reionize the universe (Nakamoto et al. 2001). On the other hand, for the latter run ($M_{halo} \simeq 6 \times 10^8 \ M_\odot$), the final stellar fraction is smaller than in the fiducial model, but the effect is not as drastic as in the former case. In this case, the final fraction of stars is ~20% smaller than in the fiducial model.

We also stress that the effect of radiation transfer is very important for such an early-reionization model. In the lower panels of Figure 12, the results from the optically thin simulations are also plotted as dashed curves. It is quite clear that star formation is almost prohibited if the optically thin condition is assumed, where the final stellar fraction is reduced

by an order of magnitude. The results of a more systematic investigation will be reported in a forthcoming paper.

4. DISCUSSION

4.1. *Substructure Problem*

Recent numerical simulations predict that subgalactic dark halos are overabundant compared to dwarf spheroidal galaxies (dSphs) observed around our Galaxy (Moore et al. 1999). So far, the possibility that this substructure problem might be reconciled if the star formation is significantly suppressed by the UVB in subgalactic halos has been discussed extensively. However, the present simulations have shown that the suppression by the UVB is not complete. In particular, even in the early-reionization regime, photoevaporation by the UVB is not complete, and the effects of self-shielding are still significant. Hence, in the context of CDM cosmology, some fraction of baryons forms stars inevitably. Thus, we have to take the shelf-shielding into account properly in order to evaluate the effects of UVB feedback on the substructure problem. To make a further approach to this problem, other issues, such as internal UV sources, evaporation driven by SN
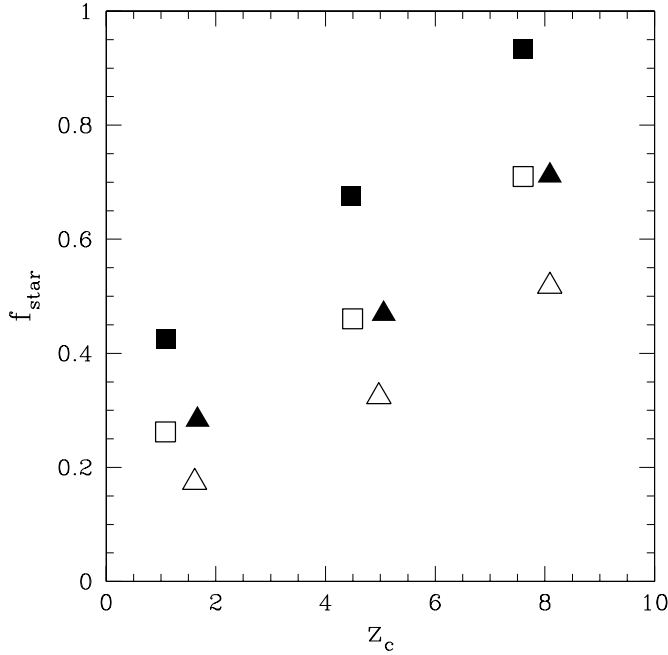
Fig. 10.—Final stellar fraction f_{star} compared between radiative transfer and optically thin cases, assuming $c_* = 0.1$. Filled symbols represent the results of full radiative transfer simulations, and open symbols denote the results of optically thin simulations.

explosions with a strongly top-heavy initial mass function of formed stars, or gas stripping in the intracluster medium, may have to be investigated.

4.2. *Dwarf Elliptical and dSph Galaxies in the Local Group*

What objects correspond to the simulated galaxies? One possibility is dwarf elliptical and dSph galaxies in the Local Group (LG). The dwarf galaxies in the LG are known to be extended (low surface brightness), spheroidal systems (e.g., Mateo 1998). In particular, faint dSphs ($M_V \gtrsim -14$) have a larger mass-to-light ratio. Hirashita, Takeuchi, & Tamura (1998) have found

$$\log(M_{vir}/L) = 2.0 \log M_{vir} + 13.1 \qquad (15)$$

for $M_{vir} < 10^8 M_\odot$, while $\log(M_{vir}/L) \simeq 0.4 - 0.7$ for $M_{vir} > 10^8 M_\odot$. These observational features indicate that the mass loss is more prominent for $M_{vir} < 10^8 M_\odot$. This can be attributed to SN-driven winds (Hirashita et al. 1998; Mori, Ferrara, & Madau 2002). The present numerical simulations suggest that such a wind can also occur by means of photo-heating due to the reionization, even before SN explosions drive a thermal wind. If we use the final stellar fraction (eq. [13]), we find $M_{halo}/L = 63$, assuming $M_{star}/L = 3$ for $z_c = 1.7$ and $M_{halo} \simeq 6 \times 10^7 M_\odot$. Such a high mass-to-light ratio is also obtained in recent results by Ricotti (2003), in which three-dimensional cosmological radiation hydro-dynamic simulations are performed with the OTVET approximation (Gnedin & Abel 2001). We also remark that Shaviv & Dekel (2003) pointed out the connection between dSphs and photoevaporated galaxies with one-dimensional simulations.

In addition, the SFH in LG dwarfs has a ubiquitous feature (e.g., Mateo 1998; Gnedin 2000a). The stars in most LG

dwarfs are estimated to have formed more than 10 Gyr ago. This means that the SFR should have a clear cutoff at such an epoch. If we assume that the age of the universe is 13 Gyr, 10 Gyr in look-back time corresponds to $z \sim 3$, which is 2 Gyr later than the cutoff epoch ($z \sim 4-5$) in the present simulations. However, the observed SFH itself should have uncertainties of a few gigayears. Thus, reheating by reionization could be one promising mechanism to provide such a cutoff in the SFH of LG dwarf galaxies. In addition, the SFH in the LG dwarfs has another important feature: there still remain weak star formation activities after the cutoff of the SFR. This feature may be reproduced by the numerical galaxies presented here, if c_* is at a level of 0.01 for relatively high mass and high z_c models (see § 3.2). Furthermore, if one incorporates the recycling of gas ejected from the stars, which is not included in the present simulation, additional stars may form, unless complete evaporation does not occur. This tendency is expected to be conspicuous for halos with a deep gravitational potential. However, the gas ejected to interstellar space in such dwarf galaxies will be photoionized again. The effects of self-shielding and the formation of dust will delay the photoevaporation of the processed gas, and consequently some amount of gas will be converted into stars again.

4.3. *Dwarf Irregular Galaxies in the LG*

On the other hand, the observed dwarf irregular galaxies (dIrrs) in the LG still have significant star formation activities embedded in old, extended, spheroidal components. Although we have no counterpart in the present simulations, we can infer the origin of such galaxies by extrapolating the numerical results. Massive ($\sim 10^{10} M_\odot$) halos formed at low z_c might be candidates for such galaxies. In such halos, small-scale perturbations grow slowly. Thus, the fraction of the gas component after the reionization of the universe is large, as seen in Figure 7. In addition, such halos have a gravitational potential deep enough to sustain photoionized gas, so that stars form efficiently from such abundant gas. Therefore, active star formation is expected even after the reionization. We can suggest that the conditions requisite for dIrr formation are (1) that the gravitational potentials of dark halos are deep enough to retain photoheated gas and (2) that the galaxy formation epoch is later than the reionization epoch. Actually, dIrrs appear to be rather massive (e.g., Mateo 1998). In addition, the reduction of the SFR due to the UVB may suppress the SN-driven galactic wind and thereby allow the formation of diffuse dwarf systems like dIrrs.

5. CONCLUSIONS

In this paper, we have performed three-dimensional radiation hydrodynamic simulations on the formation of low-mass objects under the UVB. The suppression by the UVB of the formation of low-mass objects at lower redshifts ($M \lesssim 10^9 M_\odot$, $z_c \lesssim 5$) is confirmed. However, simultaneously it is found that the formation of low-mass galaxies at low redshifts is not completely forbidden by UVB-induced photoevaporation. Baryons at high-density peaks can collapse and be self-shielded from the UVB even during the reionization, to form stars eventually. This occurs even if the universe was reionized at earlier epochs, as suggested by the *WMAP*. Thus, the effects of UVB feedback on the substructure problem in a cold dark matter (CDM) scenario should be evaluated with careful treatment of the radiative transfer.
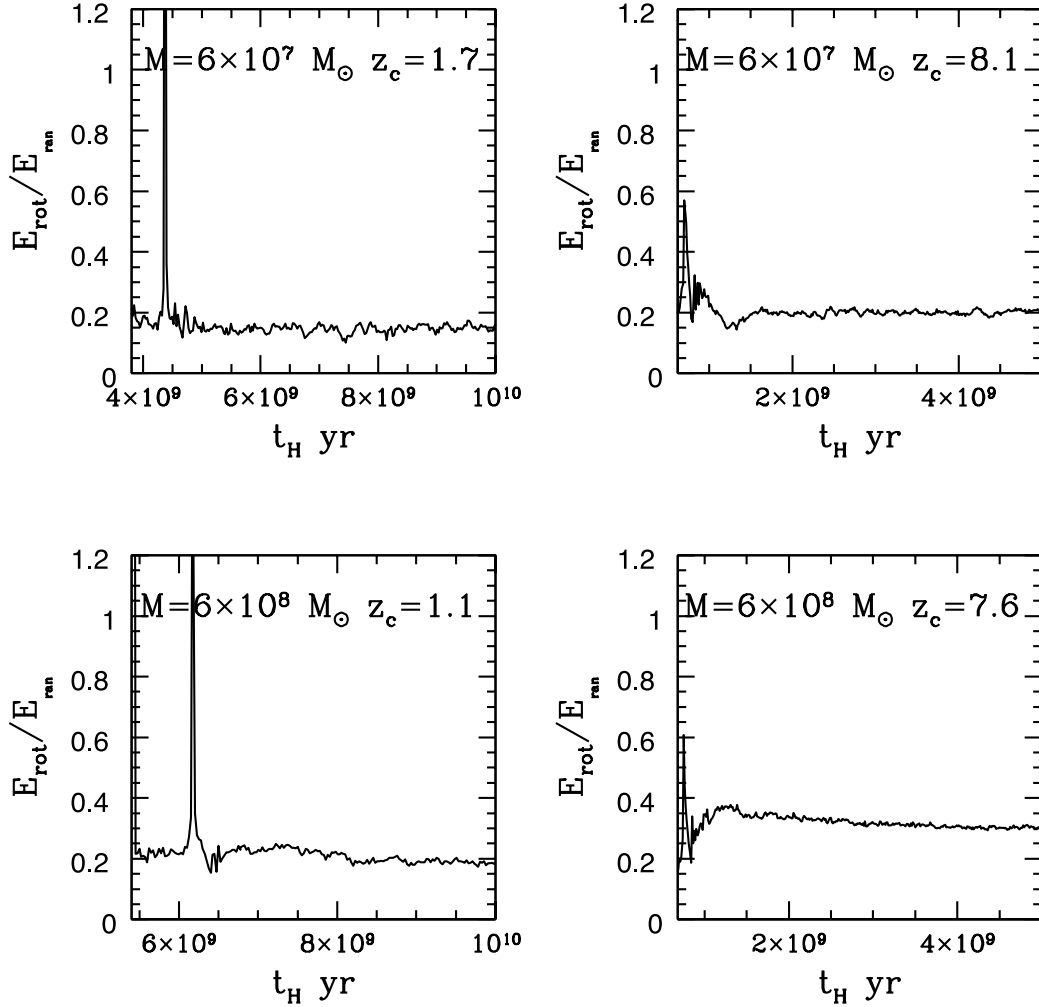
FIG. 11.—Rotation energy–to–random motion energy ratio (E_{rot}/E_{ran}) vs. cosmic time. Parameters for the panels are the same as in Fig. 6. Spikes in this figure come from the merger of subclumps. Since E_{rot} and E_{ran} are measured from the center of gravity (see the text), violent mergers cause high spikes. Especially in the left panels, the collapse epoch is relatively late, so that such violent merger phases are conspicuous.

In order to clarify the effects of radiative transfer, we have compared the results of these simulations with those obtained under the assumption of an optically thin medium. The reduction for the final stellar fraction is 30%–40% without radiative transfer in the $z_{reion} \simeq 7$ regime. Hence, the star formation before the reionization is important in determining the final stellar fraction. However, the radiative transfer effect is much more serious in the earlier reionization ($z_{reion} \simeq 17$) regime, in which the reduction for the final stellar fraction is more than an order of magnitude. In addition, it should be stressed that in the optically thin approximation, the gas temperature of the cloud always becomes higher than 10^4 K after the reionization, so that stars cannot form there, whereas the self-shielding arising from radiative transfer allows star formation, even after the reionization, if the gravitational potential is deep enough to retain the gas. The star formation after the reionization must influence the subsequent evolution of dwarf galaxies with the possible recycling of interstellar matter.

In the previous optically thin simulations (e.g., Tassis et al. 2003), the star formation criteria are different from those in the present simulation. The conditions used here are stricter than those used in previous works. In previous simulations, stars can form slowly even after the reionization because of the milder star formation conditions, although the cold H I regions cannot be formed. Although such a treatment of star formation might be approximately valid, it should be confirmed by the simulations with radiative transfer.

We have also investigated the effects of c_* and found that the final stellar fractions are not as different for various values of c_*. However, a smaller value of c_* delays star formation and allows enhanced star formation after the reionization, if the system is relatively massive and the collapse epoch is considerably later than the reionization. In addition, if the stellar feedback is taken into account, further effects of c_* may be expected, since (1) a larger c_* results in faster recycling (i.e., a larger amount of heavy elements), and (2) a larger c_* is followed by simultaneous SN explosions, which means easier disruption of host galaxies. These issues should be investigated by simulations that take into account stellar feedback coupled with radiative transfer.

The star clusters formed at high-density peaks coalesce with each other in a dissipationless fashion to form a spheroidal system with a large mass-to-light ratio. It is also found that there is a sharp cutoff of the SFR at $z \simeq 4$–5 in all the simulations because of the appreciable photoevaporation of cold gas clouds in the reionized universe. Moreover, in
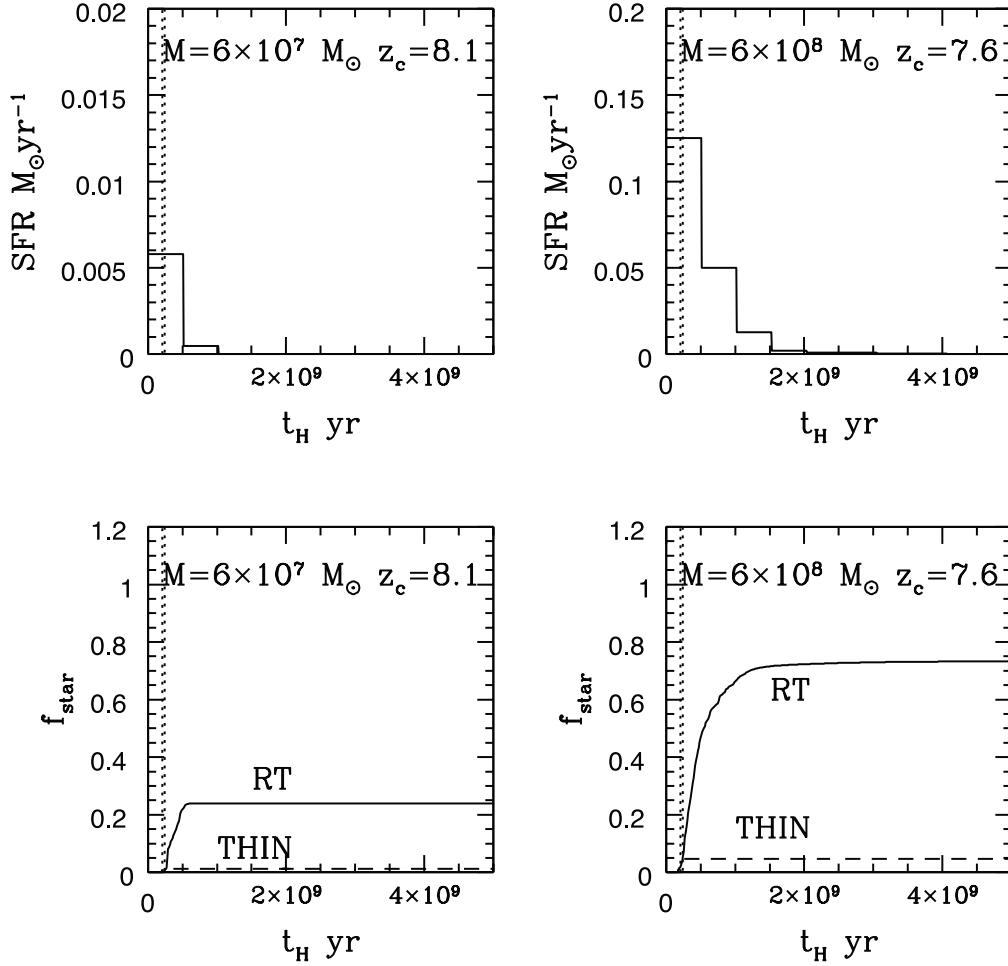
FIG. 12.—SFHs in the early-reionization regime (*top*) and time evolutions of the stellar fraction (*solid curves, bottom*). The parameters are displayed in each panel. The results of optically thin simulations are also shown in the bottom panels (*dashed curve*). In these simulations, $c_* = 0.1$ is assumed. The vertical dashed lines denote $z = 17$ and 16, between which the reionization is almost completed in this early-reionization model.

massive dwarf galaxies ($M_{\rm halo} \simeq 6 \times 10^8\ M_\odot$) formed at high redshifts ($z_c \sim 8$), weak star formation activities continue even after the reionization. On the other hand, less massive ($M_{\rm halo} \simeq 6 \times 10^7\ M_\odot$) galaxies formed later ($z_c \lesssim 8$) do not have star formation activities after $z \simeq 4$–5. Observational counterparts of these systems might be the dwarf spheroidal galaxies in the Local Group. Those galaxies have extended, old, and spheroidal stellar systems with characteristic SFHs. It is also known that fainter galaxies have larger mass-to-light ratios. All of those features agree qualitatively with those of the simulated galaxies, although the stellar feedback should also be investigated to make quantitative comparisons with observed galaxies.

APPENDIX

TESTS FOR THE NUMERICAL SCHEME

Here we show some tests of the present numerical scheme. Using this scheme, we tested the propagation of the ionization front in a uniform medium. The test results are shown in Figures 13 and 14, in which several snapshots of the ionization structures and temperature distributions are shown. In this test, a uniform cube is irradiated from the left by the ionization flux, which is proportional to ν^{-1}. The initial (neutral) optical depth of each SPH particle at the Lyman limit is $\sim 10^3$. The vertical axis denotes the fraction of electrons (Fig. 13) or temperature (Fig. 14), and the horizontal axis shows the normalized size of the cube. The position of the particles are located at the grid points. The axes of the grid are set so that they are not parallel or perpendicular to the surfaces of the cube. The vertices denote the ionization structure at four different times by the RSPH code,
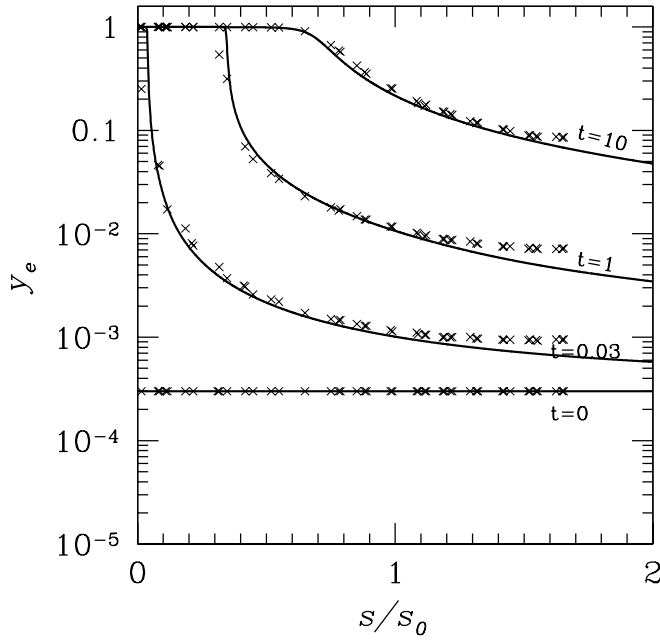
FIG. 13.—Propagation of the ionization front (also see the text). Crosses denote the numerical results with RSPH, while solid lines are for the results obtained by the one-dimensional mesh code described in the text. [*See the electronic edition of the Journal for a color version of this figure.*]
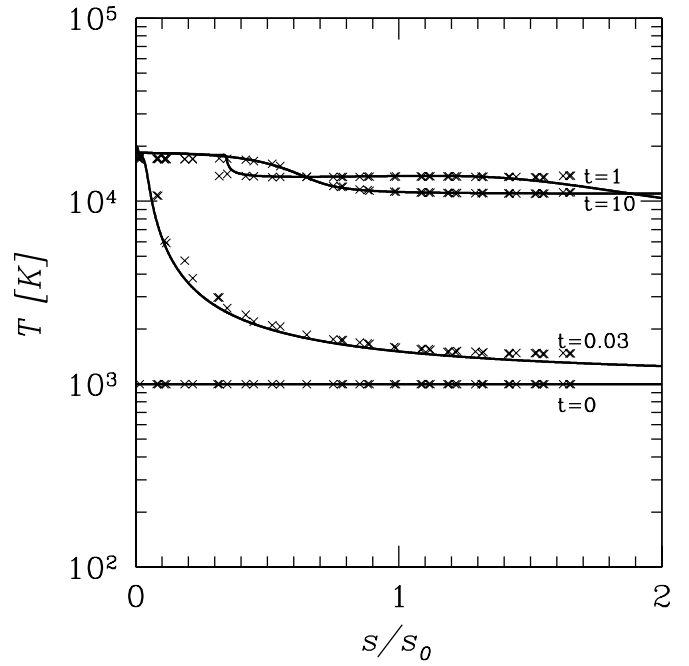
FIG. 14.—Same as Fig. 13, except that the vertical axis denotes gas temperature. [*See the electronic edition of the Journal for a color version of this figure.*]

and the four solid lines denote the results obtained by a one-dimensional mesh code, which uses 2×10^5 meshes (this number of meshes corresponds to $\delta\tau \sim 0.1$ at the Lyman limit, which is enough to resolve the ionization front). It is quite clear that the RSPH scheme can reproduce the propagation of ionization structure fairly well, although the optical depth of an SPH particle is much larger than unity.

REFERENCES

Abel, T., Norman, M. L., & Madau, P. 1999, ApJ, 523, 66
Babul, A., & Rees, M. J. 1992, MNRAS, 255, 346
Bajtlik, S., Duncan, R. C., & Ostriker, J. P. 1988, ApJ, 327, 570
Binney, J., Gerhard, O., & Silk, J. 2001, MNRAS, 321, 471
Boku, T., Makino, J., Susa, H., Umemura, M., Fukushige, T., & Ukawa, A. 2002, IPSJ Trans. High Performance Computing Syst., 43, 6
Bromm, V., Ferrara, A., Coppi, P. S., & Larson, R. B. 2001, MNRAS, 328, 969
Cen, R., & Ostriker, J. P. 1993, ApJ, 417, 404
Cole, S., Aragón-Salamanca, A., Frenk, C. S., Navarro, J. F., & Zepf, S. E. 1994, MNRAS, 271, 781
Corbelli, E., Galli, D., & Palla, F. 1997, ApJ, 487, L53
Dalgarno, A., & McCray, R. A. 1972, ARA&A, 10, 375
Dekel, A., & Rees, M. J. 1987, Nature, 326, 455
Djorgovski, S. G., Castro, S., Stern, D., & Mahabal, A. A. 2001, ApJ, 560, L5
Dove, J. B., & Shull, J. M. 1994, ApJ, 423, 196
Efstathiou, G. 1992, MNRAS, 256, 43P
Ferrara, A., & Tolstoy, E. 2000, MNRAS, 313, 291
Fuller, T. M., & Couchman, H. M. P. 2000, ApJ, 544, 6
Galli, D., & Palla, F. 1998, A&A, 335, 403
Giallongo, E., Cristiani, S., D'Odorico, S., Fontana, A., & Savaglio, S. 1996, ApJ, 466, 46
Gnedin, N. Y. 2000a, ApJ, 535, L75
———. 2000b, ApJ, 542, 535
Gnedin, N. Y., & Abel, T. 2001, NewA, 6, 437
Heavens, A., & Peacock, J. 1988, MNRAS, 232, 339
Hirashita, H., Takeuchi, T. T., & Tamura, N. 1998, ApJ, 504, L83
Hollenbach, D., & McKee, C. F. 1979, ApJS, 41, 555
Iwasaki, Y. 1998, Nucl. Phys. B (Proc. Suppl.), 60, 246
Kang, H., & Shapiro, P. R. 1992, ApJ, 386, 432
Kauffmann, G., White, S. D. M., & Guiderdoni, B. 1993, MNRAS, 264, 201
Kennicutt, R. C., Jr. 1998, ARA&A, 36, 189
Kessel-Deynet, O., & Burkert, A. 2000, MNRAS, 315, 713
Kitayama, T., Susa, H., Umemura, M., & Ikeuchi, S. 2001, MNRAS, 326, 1353
Koda, J., Sofue, Y., & Wada, K. 2000, ApJ, 532, 214

Kogut, A., et al. 2003, ApJS, 148, 161
Lepp, S., & Shull, J. M. 1983, ApJ, 270, 578
Makino, J. 2002, in ASP Conf. Ser. 263, Stellar Collisions, Mergers, and their Consequences, ed. M. M. Shara (San Francisco: ASP), 389
Maloney, P. 1993, ApJ, 414, 41
Mateo, M. L. 1998, ARA&A, 36, 435
Moore, B., Ghigna, S., Governato, F., Lake, G., Quinn, T., Stadel, J., & Tozzi, P. 1999, ApJ, 524, L19
Mori, M., Ferrara, A., & Madau, P. 2002, ApJ, 571, 40
Nakamoto, T., Umemura, M., & Susa, H. 2001, MNRAS, 321, 593
Nishi, R., & Susa, H. 1999, ApJ, 523, L103
Omukai, K. 2000, ApJ, 534, 809
Razoumov, A. O., Norman, M. L., Abel, T., & Scott, D. 2002, ApJ, 572, 695
Ricotti, M. 2003, in The IGM/Galaxy Connection: The Distribution of Baryons at $z = 0$, ed. J. L. Rosenberg & M. E. Putman (Dordrecht: Kluwer), 193
Ricotti, M., Gnedin, N. Y., & Shull, J. M. 2002a, ApJ, 575, 33
———. 2002b, ApJ, 575, 49
Schneider, R., Ferrara, A., Natarajan, P., & Omukai, K. 2002, ApJ, 571, 30
Shapiro, P. R., & Raga, A. C. 2001, in Rev. Mexicana Astron. Astrofis. Ser. Conf. 10, The Seventh Texas-Mexico Conference on Astrophysics: Flows, Blows and Glows, ed. W. H. Lee & S. Torres-Peimbert (Mexico, DF: Inst. Astron., UNAM), 109
Shaviv, N. J., & Dekel, A. 2003, MNRAS, submitted (astro-ph/0305527)
Songaila, A. 2001, ApJ, 561, L153
Steinmetz, M., & Bartelmann, M. 1995, MNRAS, 272, 570
Steinmetz, M., & Müller, E. 1993, A&A, 268, 391
Sugimoto, D., Chikada, Y., Makino, J., Ito, T., Ebisuzaki, T., & Umemura, M. 1990, Nature, 345, 33
Susa, H., & Kitayama, T. 2000, MNRAS, 317, 175
Susa, H., & Umemura, M. 2000a, ApJ, 537, 578
———. 2000b, MNRAS, 316, L17
Tajiri, Y., & Umemura, M. 1998, ApJ, 502, 59
Tassis, K., Abel, T., Bryan, G. L., & Norman, M. L. 2003, ApJ, 587, 13
Tegmark, M., Silk, J., Rees, M. J., Blanchard, A., Abel, T., & Palla, F. 1997, ApJ, 474, 1

Thacker, R. J., Tittley, E. R., Pearce, F. R., Couchman, H. M. P., & Thomas, P. A. 2000, MNRAS, 319, 619
Thoul, A. A., & Weinberg, D. H. 1996, ApJ, 465, 608
Umemura, M. 1993, ApJ, 406, 361
Umemura, M., Fukushige, T., Makino, J., Ebisuzaki, T., Sugimoto, D., Turner, E. L., & Loeb, A. 1993, PASJ, 45, 311
Umemura, M., & Ikeuchi, S. 1984, Prog. Theor. Phys., 72, 47

Umemura, M., Nakamoto, T., & Susa H. 2001, in ASP Conf. Ser. 222, The Physics of Galaxy Formation, ed. M. Umemura & H. Susa (San Francisco: ASP), 109
White, S. D. M., & Frenk, C. S. 1991, ApJ, 379, 52
Young, L. M., & Lo, K. Y. 1997a, ApJ, 476, 127
———. 1997b, ApJ, 490, 710